Journal of Microscopy

Journal of Microscopy, 2011
Received 18 October 2010; accepted 19 December 2010
doi: 10.1111/j.1365-2818.2010.03484.x

Transmission electron microscopy with a liquid flow cell

K.L. KLEIN*, I.M. ANDERSON* & N. DE JONGE†
**Surface and Microanalysis Science Division, National Institute of Standards and Technology, Gaithersburg, Maryland, U.S.A.*
†Department of Molecular Physiology and Biophysics, Vanderbilt University School of Medicine, Tennessee, U.S.A.

Key words. Chromatic aberration, *in situ*, liquid, nanoparticles, spatial resolution, STEM, TEM.

Summary

The imaging of microscopic structures at nanometre-scale spatial resolution in a liquid environment is of interest for a wide range of studies. Recently, a liquid flow transmission electron microscopy (TEM) holder equipped with a microfluidic cell has been developed and shown to exhibit flow of nanoparticles through an electron transparent viewing window. Here we demonstrate the application of the flow cell system for both scanning and conventional transmission electron microscopy imaging of immobilized nanoparticles with a resolution of a few nanometres in liquid water of micrometre thickness. The spatial resolution of conventional TEM bright field imaging is shown to be limited by chromatic aberration due to multiple inelastic scattering in the water, and we demonstrate that the liquid in the cell can be displaced by a gas phase that forms under intense electron irradiation. Our data suggest that under appropriate conditions, TEM imaging with a liquid flow cell is a promising method for understanding the *in situ* behaviour of nanoscale structures in a prescribed and dynamically changing chemical environment.

Introduction

The electron optical imaging of microscopic structures in a hydrated state, and biological specimens in particular, dates from the initial development of the electron microscope (Marton, 1935). Strategies for the electron optical imaging of hydrated specimens include the use of differentially pumped sample chambers (Danilatos & Robinson, 1979) or thin membranes to enclose the 'wet' environment inside the vacuum of the electron microscope (Parsons, 1974; Daulton *et al.*, 2001; Liu *et al.*, 2008). Williamson *et al.* (2003) were the first to report TEM analysis of nanoscale structures within an enclosed cell where liquid filled a viewing area between two electrodes by capillary action. This technique was used to record the nucleation and growth of nanoscale copper clusters during electrodeposition. Later, this same closed cell technique was applied to study nanocrystal diffusion and growth in solution with the aid of electron beam heating (Zheng *et al.*, 2009a,b). Liquid enclosures were also developed for the scanning electron microscope (SEM) (Thiberge *et al.*, 2004; Nishiyama *et al.*, 2010).

Recently, de Jonge *et al.* (2009) have used a liquid flow holder equipped with a microfluidic cell to perform scanning transmission electron microscopy (STEM) high-angle annular dark field (HAADF) imaging of whole eukaryotic cells labelled with high atomic number (Z) gold nanoparticles in several micrometres of flowing liquid. Earlier implementations of impermeable cells that allowed mass transport were used to flow vapour, rather than liquid, to and from the viewing area, with consequently limited applications (Daulton *et al.*, 2001). Our microfluidic cell has recently been shown to allow the dynamic flow of nanoparticles (Ring & de Jonge, 2010). Electron optical imaging of hydrated structures in flowing liquid provides a distinct advantage relative to similar analyses carried out in the static liquid environment of a closed cell, or alternatively cryogenic electron microscopy of frozen hydrated specimens, because the chemical environment can be prescribed and changed dynamically during the experiment via the flowing liquid. Confocal optical microscopy is another valuable technique that provides the advantage of dynamic flow, but the spatial resolution is limited to a scale of the order of the photon wavelength, typically greater than 100 nm. The liquid flow cell affords additional ancillary advantages for electron microscopy studies. In contrast to a closed cell without any active flow mechanism, the continuous flow of liquid better ensures that the entire sample compartment fills with fluid, which is not lost via leakage and evaporation during the course of the experiment. Also, the flow of liquid can be used to help mitigate the formation of charge and/or temperature gradients that may accumulate while imaging

Correspondence to: K.L. Klein, Surface and Microanalysis Science Division, National Institute of Standards and Technology, 100 Bureau Drive, Gaithersburg, MD 20899-8371, U.S.A. Tel: +1-301-975-8090; e-mail: kate.klein@nist.gov

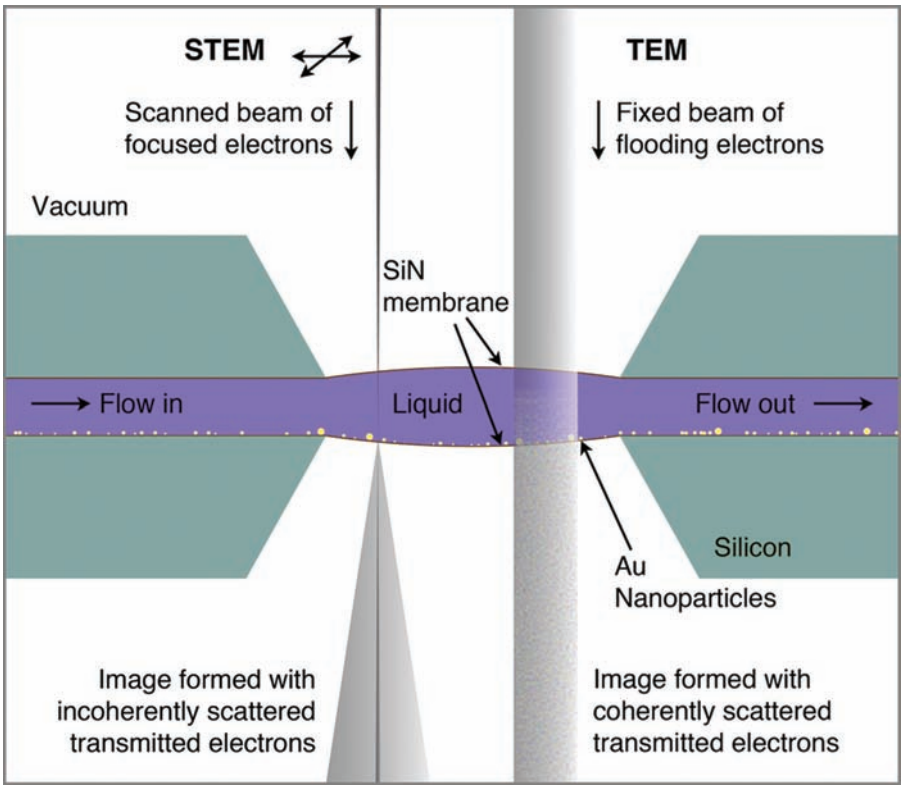

Fig. 1. Schematic representation of liquid STEM and TEM imaging of gold nanoparticles located on the beam exit membrane window of a microfluidic cell.

with an electron beam. Finally, fluid flow also makes possible the exchange of specimens in solution for continuous flow studies and collection of particle statistics.

Transmission electron microscopy provides flexibility in the selection of an imaging mode and contrast formation mechanism that is tailored to a given study. For example, conventional TEM, with its higher beam current, has the potential to capture data more quickly than a STEM image of the same number of pixels, with consequent advantages for dynamic measurements. STEM or TEM may be more advantageous for a given application, depending upon the critical damage mechanisms and the dose or dose rate sensitivity of the specimen. The incoherent contrast of HAADF imaging (typically used in STEM mode) is well suited for the imaging of nanoparticle labels composed of high-Z elements, whereas the coherent contrast of bright field imaging (typically used in TEM mode) allows for simultaneous imaging of high- and low-Z materials, such as a nanoparticle functionalized with a macromolecule.

Here we report the imaging of nanoparticles in a liquid flow cell using both STEM and TEM techniques, as shown schematically in Fig. 1. This paper presents an overview of the TEM approach and some preliminary observations concerning bright field imaging of gold nanoparticles through a saline water layer of micrometre-scale thickness. Data were acquired using a microfluidic cell, composed of two silicon microchips with electron transparent silicon nitride windows, that interfaced with a prototype fluid flow holder providing fluid circulation through the cell from the outside of the electron microscope.

Materials and methods[1]

The liquid flow holder and its key components were manufactured by Protochips Inc. and are shown in Fig. 2. The liquid flow is generated by a Harvard Apparatus syringe pump assembly, which delivers a controlled flow rate to the TEM holder through the inlet plastic tubing from a filled syringe; a second outlet tube allows the flow of waste fluid from the holder (Fig. 2a). Corresponding internal plumbing within the liquid flow holder transfers the fluid to and from either side of a small reservoir at the tip of the specimen holder, between which are immersed the two microchips (Fig. 2b) equipped with electron transparent silicon nitride windows that form the microfluidic cell. Polystyrene microspheres of a given diameter are placed

[1] Certain commercial equipment, instruments or materials are identified in the document. Such identification does not imply recommendation or endorsement by the National Institute of Standards and Technology, nor does it imply that the products are necessarily the best available for the purpose.

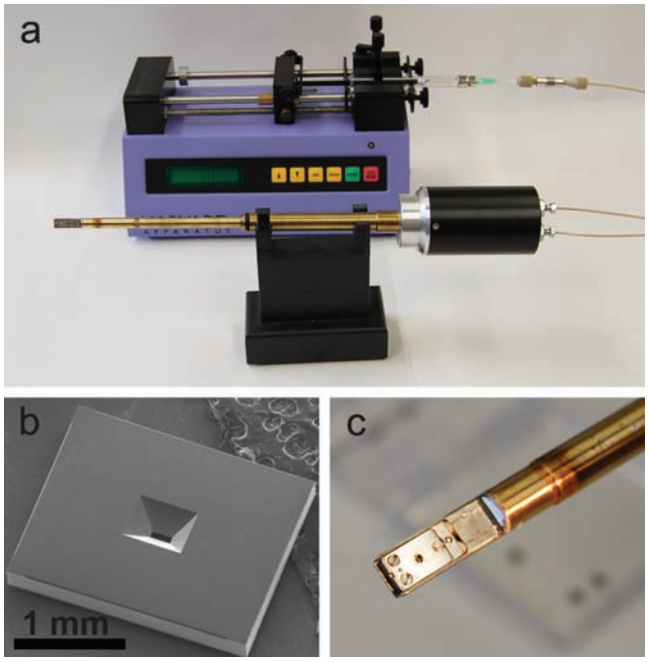

Fig. 2. The liquid flow TEM holder and its components: (a) the liquid flow specimen holder (foreground) and syringe pump assembly (background); (b) a microchip with a silicon-nitride window; and (c) the microchip assembly is encapsulated within the tip of the liquid flow TEM holder by a screw-secured plate.

between the microchips to specify the height of the microfluidic cell. The microchip assembly is sealed within the tip of the liquid flow TEM holder by a screw-secured plate having a small aperture that allows electron beam access to the silicon nitride windows (Fig. 2c). O-ring seals are used to isolate the fluid-filled chamber from the high vacuum of the microscope. With this configuration, the liquid flow is accommodated via two channels, both through and around the microfluidic cell in proportion to their relative transmittance; only a small fraction of the flow is transmitted through the narrow microfluidic cell.

The microfluidic flow cell consists of two custom-designed silicon microchips (de Jonge *et al.*, 2009), which has recently been shown to allow the dynamic flow of nanoparticles (Ring & de Jonge, 2010). At the centre of each chip is a 50 μm × 200 μm window made of a 50-nm-thick low-stress silicon nitride membrane. Before use, the microchips were cleaned thoroughly with high-pressure liquid chromatography grade acetone and ethanol to remove resist material and residues from the fabrication process. Following the solvent cleaning, a dilute solution of 2-μm-diameter polystyrene microspheres was deposited as 0.1 μL droplets at each corner of the membrane side of one of the two microchips. Because the solvent cleaning renders the surface of the microchip hydrophobic, the small droplets do not wet the surface and remained in place as they dry, concentrating the microspheres where they have been deposited. Before loading the TEM holder, the two microchips (one with the microsphere spacer and one without) that together compose the cell were plasma cleaned to render the membrane surfaces hydrophilic for the fluid flow experiments.

A 0.5 μL droplet of a solution composed of nominally 10 nm (NIST Reference Material 8011, citrate stabilized) and 1.4 nm (Nanoprobes Nanogold Labeling Reagents) diameter gold nanoparticles was dispensed onto the electron-transparent window area of one of the two microchips. After drying, the dispersion of particles on the membrane was verified by STEM-HAADF imaging. The microchip and its mate were then loaded into the liquid flow TEM holder with a 0.8 μL droplet of diluted (10% in high-pressure liquid chromatography grade water) phosphate buffered saline (PBS) solution (ATCC Dulbecco's formulation: NaCl, 8 g/L; $Na_2HPO_4{\cdot}7H_2O$, 2.16 g/L; KCl, 0.2 g/L; KH_2PO_4, 0.2 g/L) sandwiched between them, which acts to prime the microfluidic cell for fluid flow. The microchip sandwich was oriented such that the gold nanoparticles were deposited within the fluidic cell at the beam-exit membrane, as shown schematically in Fig. 1. The wetting of both chip surfaces took place due to the hydrophilicity of the membranes following plasma cleaning. The lid of the specimen holder was then secured with screws to form a vacuum seal as shown in Fig. 2(c). The flow of buffer solution via the syringe pump was set to 50 nL s^{-1} and the flow through the circuit was verified by observing drops of liquid exiting the outlet tubing. The specimen holder was visually checked for leaks under an optical microscope and then loaded into the goniometer stage of the electron microscope. After loading the liquid flow cell holder, the vacuum level in the column was monitored to ensure that there was no detectable leaking of fluid from the cell before opening the valve isolating the column from the electron gun.

The aqueous nanoparticles were imaged using a Philips/FEI CM200FEG STEM/TEM operating at 200 kV. Imaging was performed in both STEM and TEM modes, as shown schematically in Fig. 1. In STEM mode, a focused beam of electrons is scanned across the specimen and an image is formed by the output of the HAADF detector, which collects transmitted electrons incoherently scattered to high angles. STEM image acquisition parameters include a probe current of 0.4 nA, (1024 × 1024) pixels × 0.9 nm per pixel, a per pixel dwell time of 20 μs, and a HAADF inner angle of $\beta =$ 70 mrad. Conversely, in TEM mode, a fixed beam of flooding electrons irradiates the relevant area of the flow cell and an image is formed with the objective lens by transmitted electrons that were coherently scattered to low angles and collected with a charge-coupled device camera. TEM imaging was performed with a beam current of 7 nA. STEM imaging achieves its highest resolution for nanoparticles positioned close to the electron beam entrance window, so that the probe is not blurred by transmission through the water (de Jonge *et al.*, 2010); conversely, TEM imaging achieves its highest resolution for nanoparticles positioned close to the

electron beam exit window, as shown schematically in Fig. 1, in accordance with the principle of reciprocity (Cowley, 1969). Both TEM and STEM imaging of nanoparticles in the fluid-filled cell were performed near the edge of the silicon nitride window, where the thickness of the fluid layer was the smallest; the thickness of the fluid layer at the centre of the window can be substantially larger due to elastic deformation of the windows under the pressure differential between the fluid-filled cell and the high vacuum of the microscope column.

Intensity profiles were extracted across selected particles of interest, using a three pixel wide integration in the direction perpendicular to the profile. The contrast of TEM bright field intensity profiles was inverted for ready comparison with comparable profiles from STEM dark field images. Both STEM and TEM images were processed for display; the image intensities were scaled to maximize the dynamic range and a 1 pixel radius median filter was used as a noise filter.

Results and discussion

STEM-HAADF images of gold nanoparticles, in both desiccated and hydrated states, are shown in Fig. 3. A high concentration of nanoparticles of both 1.4 nm and 10 nm diameter are visible with high contrast on a discontinuous background contributed by the dried residue of the dispensing solution when desiccated (Fig 3a). Although the intensity of the smaller particles indicated in Fig. 3(a) is comparable to the intensity of the residue at its thickest, the presence of these particles is distinguished by their high intensity localized to a region of a few nanometres diameter, which arises because of the significantly greater atomic number ($Z = 79$) of the gold particles relative to all elements in the organic solution (maximum $Z = 8$ for oxygen) and the high atomic number dependence (approaching the Z^2 dependence of the Rutherford cross section) of HAADF imaging. In the flowing liquid, the nanoparticles exhibit relatively low contrast against the homogeneous background contributed by multiple elastic scattering from the aqueous solvent (Fig. 3b). Nanoparticles of both 1.4 and 10 nm diameters are evident as well as a nanoparticle of 20 nm diameter, which may represent an outlier or the agglomeration of smaller particles. The nanoparticles are in lower concentration than observed on the dried membrane, presumably due to desorption and dispersal by the fluid.

The thickness of the fluid layer was estimated by measuring the ratio of beam currents scattered onto the HAADF detector, N, to the incident beam current, N_0 (de Jonge *et al.*, 2010). The thickness of the liquid, t, follows from this ratio according to the Poisson probability distribution function (Reimer & Kohl, 2008)

$$t = -\lambda(\beta)\ln\left[1 - \frac{N}{N_0}\right] \approx \lambda(\beta)\frac{N}{N_0}, \qquad (1)$$

where $\lambda(\beta)$ is the mean-free-path for elastic scattering to semi-angles greater than β, the inner angle of the HAADF detector. This formula assumes that multiple scattering to

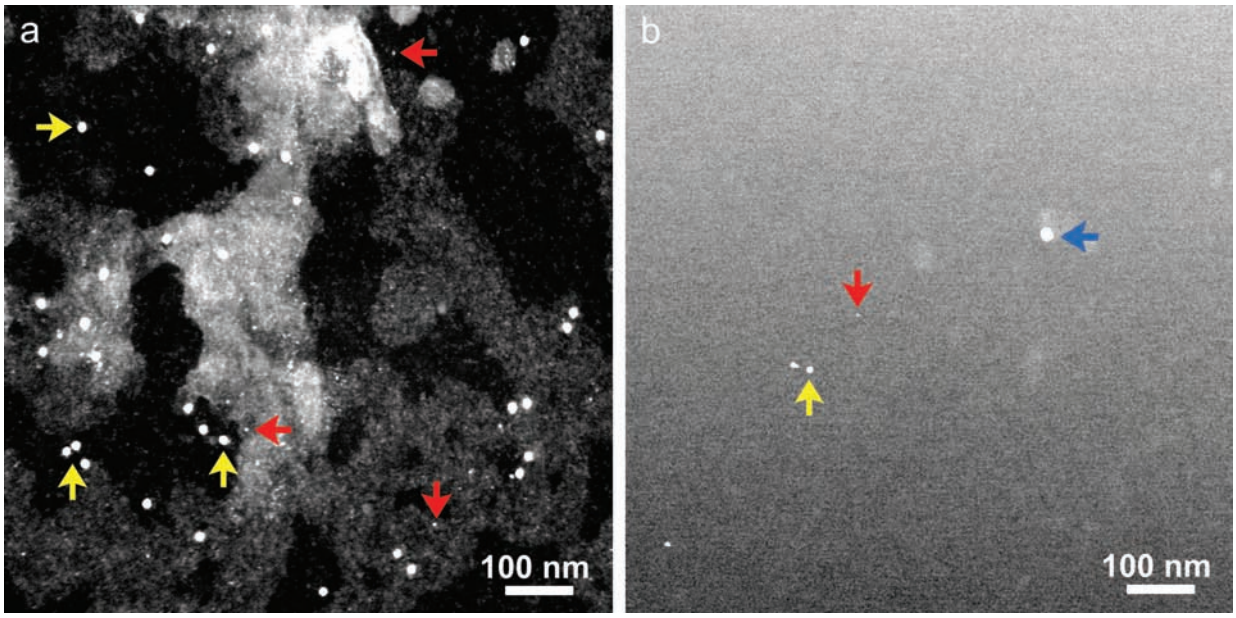

Fig. 3. STEM images of the assortment of gold nanoparticles: (a) imaged under high vacuum as a dried dispersion on the silicon nitride membrane; and (b) imaged through ≈0.8 μm of liquid after rehydration in the microfluidic cell. Three different diameter nanoparticles (1.4 nm, 10 nm and 20 nm) are indicated in the image by red, yellow and blue arrows, respectively. Saturation of the intensity for the 10-nm-diameter particles in (a), necessary to improve the visibility of the 1.4 nm diameter particles against the high background of the residue, accounts for the larger apparent size of the particles relative to those in (b).

angles higher than the outer semi-angle ($\approx 2\beta$) of the HAADF detector is negligible; given the weak high-angle scattering of low Z elements, this assumption was deemed reasonable in the low thickness regime where the approximate formula holds. Indeed, this method has been previously shown to agree with other thickness measurement techniques to within 20% (de Jonge *et al.,* 2010). A water thickness of $t \approx 0.8$ μm was determined, based on a calculated value of $\lambda_{water} = 10.5$ μm for $\beta = 70$ mrad (de Jonge *et al.,* 2009). This thickness is smaller than the diameter of the 2 μm microsphere spacer, presumably due to compression of the microspheres or bending of the microchips from tightening the screws on the holder lid, which has been observed in earlier work (de Jonge *et al.,* 2009, 2010).

The spatial resolution of STEM-HAADF imaging in 0.8 μm of fluid was sufficient to identify gold nanoparticles of 1.4 nm diameter. The full-width at half-maximum (FWHM) of the image intensity from the smallest particle (indicated by the red arrow in Fig. 3b) was 3 nm. This profile width is consistent with the calculated broadening of the electron probe by interaction of the electron beam with the liquid. Monte Carlo simulations suggest a probe broadening solely due to interaction with the liquid of 2.5 nm FWHM for 0.8 μm thickness (de Jonge *et al.,* 2010). For the NIST 10-nm-diameter gold nanoparticle reference material, the measured FWHM of 9 nm is in good agreement with the reported mean diameter as measured by TEM of 8.9 nm, with the distribution of individual measurements exhibiting a FWHM of ≈1.4 nm (NIST RM 8011, 2007). More generally, the measured FWHMs of 3 nm and 9 nm are consistent with the convolution of the probe broadening with deposited particle diameters of 1.4 nm and 8.9 nm, respectively, because the measured profile widths represent the probe or particle diameter, depending upon whether the particle is small or large compared with the probe size.

TEM bright field images of the gold nanoparticles are shown in Fig. 4. The gold nanoparticles appear dark against the bright background of the water-filled cell, as evident at lower magnification (Fig. 4a), and exhibit a combination of amplitude and diffraction contrast. Diffraction contrast manifests itself in the appearance of intensity variations, particularly in larger particles, that are inconsistent with the smooth, symmetric variation that would be expected from an incoherent signal; such variations in the gold particle can be seen both in the bright field image (Fig. 4b) and the corresponding inverted intensity profile (Fig. 4e).

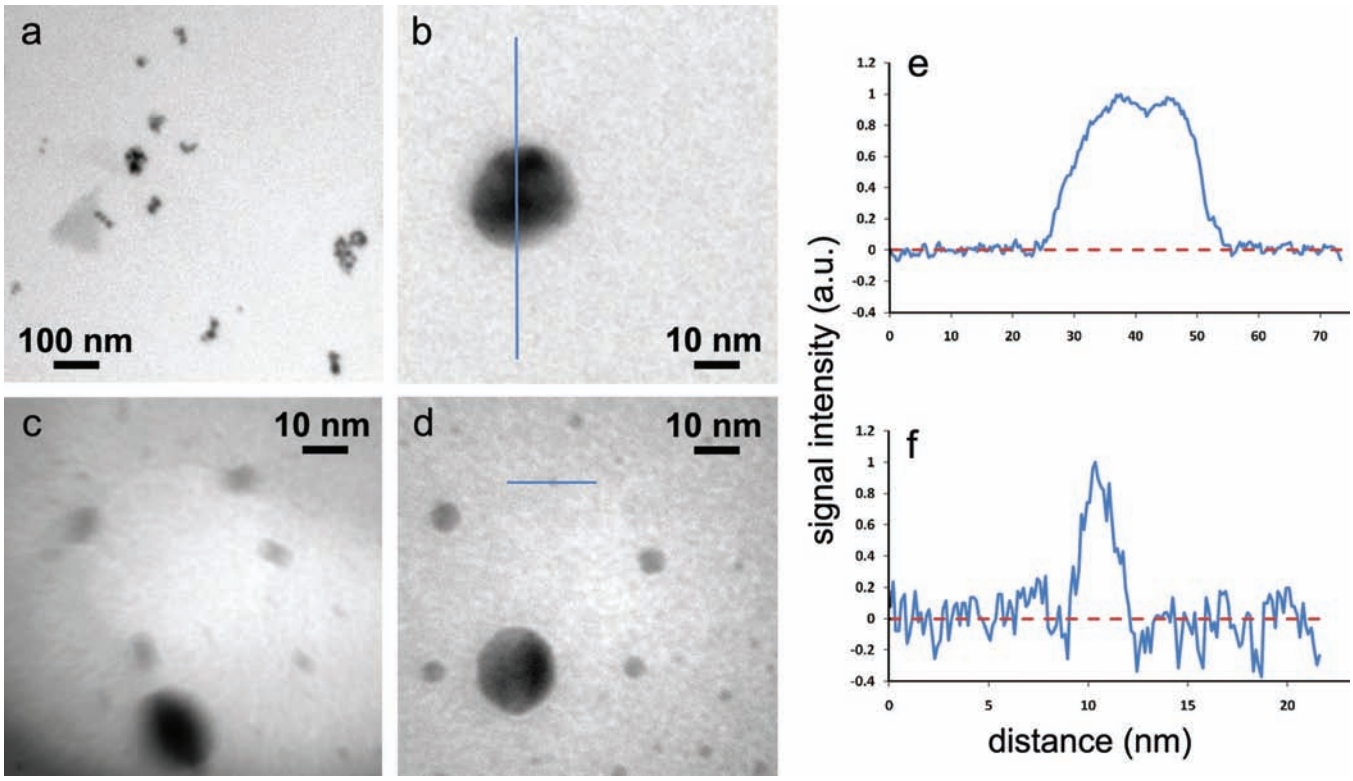

Fig. 4. Conventional TEM bright field images and inverted intensity line profiles of gold nanoparticles positioned within the microfluidic cell at the beam exit surface: (a) lower-magnification survey image of clusters of nanoparticles of different sizes; (b) higher-magnification image of an individual nanoparticle with a diameter of ≈20 nm; (c) image acquired during a beam-induced partial displacement of the fluid at higher electron dose; (d) image of the same region in (c) after uniform displacement of the majority of fluid; and (e and f) inverted intensity profiles from particles indicated in (b) and (d), respectively.

An estimate of the spatial resolution in the presence of the liquid can be ascertained from the profile in Fig. 4(e). The width of the intensity rise from 25% to 75% of the maximum across a sharp boundary provides a conservative measure of the resolution for objects that are large in comparison with the point spread function (Reimer, 1985). For a spherical particle, it can be calculated that the change in mass thickness over these limits occurs over a width equivalent to ≈15% of the particle diameter, or ≈3 nm for a 20-nm-diameter particle. This theoretical width is significantly smaller than that measured, ≈5 nm when averaged on either side of the profile, suggesting a spatial resolution of a few nanometres, which may account for the absence of the 1.4-nm-diameter particles in the images acquired from the liquid-filled cell. The observed resolution is consistent with the limiting effects of chromatic aberration, d_c, which is proportional to the range of energies ΔE substantially contributing to the image: $d_c = C_c \beta \Delta E / E_0$, where C_c is the chromatic aberration coefficient of the image-forming lens, β is the objective aperture semi-angle and E_0 is the incident beam energy, suitably corrected for relativity (Reimer & Kohl, 2008), given that multiple inelastic scattering of the transmitted electrons in the fluid increases ΔE from the nominally 1 eV of the electron source for thin specimens to two or three times the energy for plasmon scattering in the fluid, or several tens of eV. The effects of chromatic aberration could be mitigated by energy-filtered imaging to reduce ΔE, but with sacrifice of total intensity, or ideally by correction of chromatic aberration, thus lowering C_c.

It was discovered that the fluid in the cell could be locally displaced by a gas phase upon intense electron irradiation effected by sufficiently condensing the beam. The turbulence in the water during this fluid displacement results in a highly distorted image, as shown in Fig. 4(c). Upon completion, the fluid displacement extends over an area of micrometer radius concentric with the beam position, so that the majority of the fluid through the thickness of the cell is expelled from the entire field of view. This again results in an undistorted image (Fig. 4d), and the 1.4-nm-diameter gold particles, which were not evident when imaging through nearly a micron of fluid (Fig. 4b), are now clearly revealed. A line profile across one such particle, shown in Fig. 4(f), demonstrates that the particle exhibits an intensity distribution clearly distinguishable from the background noise in the image following fluid displacement. A measured FWHM of 1.7 nm indicates that there is negligible loss of resolution due to scattering in the gas.

The nature of the gas phase that forms under intense electron beam irradiation remains to be determined. It is conceivable that the fluid is displaced by the vaporization of some of the water due to the heating effects of the intense focused electron beam. An alternative possibility is that the intense electron beam hydrolyses the water, and that the gas phase is a mixture of vapour-saturated hydrogen and oxygen gases. In either event, the observed fluid displacement complicates the goal of maintaining a prescribed chemical environment, and may indicate an upper limit on the allowable electron intensity, and consequently the achievable temporal resolution for dynamic experiments that realize sufficient signal for characterization.

Conclusions and future outlook

TEM bright field imaging provides a complementary imaging mode to STEM-HAADF imaging for the study of nanoscale structures in a liquid environment. The higher beam current typical of TEM mode is potentially advantageous for dynamic imaging at faster frame rates; however, this advantage can be undermined by the displacement of fluid under the electron beam if the incident intensity is too high. Nanometer-diameter particles evident in STEM-HAADF imaging in a fluid layer of micrometer thickness were not evident in standard TEM bright field imaging due to the effects of chromatic aberration. Continuing investigation will explore the limiting effects of chromatic aberration on the resolution of TEM imaging in a liquid environment, and its mitigation using energy filtering or chromatic aberration correction. TEM imaging using a liquid flow holder offers several potential benefits relative to a closed cell configuration; most notably, mass transport enables the chemical environment to be prescribed and dynamically changed during an experiment.

Acknowledgements

The authors thank Dr. Jim Bentley of Oak Ridge National Laboratory (ORNL) for technical assistance in support of these studies. Research was supported by the National Research Council Postdoctoral Research Associateship Program (KLK) and by grant 1R43EB008589 to Dr. Stephen Mick from the National Institutes of Health (NdJ). The authors are grateful to Protochips Inc. for access to the prototype liquid flow TEM holder and material support. Electron microscopy was performed at the ORNL SHaRE User Facility, sponsored by the Division of Scientific User Facilities, Office of Basic Energy Sciences, U.S. Department of Energy.

References

Cowley, J.M. (1969) Image contrast in a transmission scanning electron microscope. *Appl. Phys. Lett.* **15**, 58.

Danilatos, G.D. & Robinson, V.N.E. (1979) Principles of scanning electron microscopy at high specimen pressures. *Scanning* **18**, 75–78.

Daulton, T.L., Little, B.J., Lowe, K. & Jones-Meehan, J. (2001) In situ environmental cell-transmission electron microscopy study of microbial reduction of chromium(VI) using electron energy loss spectroscopy. *Microsc. Microanal.* **7**, 470–485.

de Jonge, N., Peckys, D.B., Kremers, G.J. & Piston, D.W. (2009) Electron microscopy of whole cells in liquid with nanometer resolution. *Proc. Natl. Acad. Sci. USA* **106**, 2159–2164.

de Jonge, N., Poirier-Demers, N., Peckys, D.B. & Drouin, D. (2010) Nanometer-resolution electron microscopy through micrometers-thick water layers. *Ultramicroscopy* **110**, 1114–1119.

Liu, K.L., Wu, C.C., Huang, Y.J., Peng, H.L., Chang, H.Y., Chang, P., Hsu, L. & Yew, T.R. (2008) Novel microchip for in situ TEM imaging of living organisms and bio-reactions in aqueous conditions. *Lab Chip* **8**, 1915–1921.

Marton, L. (1935) Electron microscopy of biological objects. II. *Bulletins de l'Academie Royal de Belgique, Class des Sciences* **21**, 553–564.

Nishiyama, H., Suga, M., Ogura, T., Maruyama, Y., Koizumi, M., Mio, K., Kitamura, S. & Sato, C. (2010) Atmospheric scanning electron microscope observes cells and tissues in open medium through silicon nitride film. *J. Struct. Biol.* **169**, 438–449.

NIST RM 8011. (2007) Reference Material 8011: Gold Nanoparticles, Nominal 10 nm Diameter. Report issued December 13, 2007. National Institute of Standards and Technology, Gaithersburg, MD, USA.

Parsons, D.F. (1974) Structure of wet specimens in electron-microscopy. *Science* **186**, 407–414.

Reimer, L. (1985) *Scanning Electron Microscopy: Physics of Image Formation and Microanalysis*, 1st edn. Springer, Heidelberg.

Reimer, L. & Kohl, H. (2008) *Transmission Electron Microscopy*, 5th edn. Springer, New York.

Ring, E.A. & de Jonge, N. (2010) Microfluidic system for transmission electron microscopy. *Microsc. Microanal.* **16**, 622–629.

Thiberge, S., Nechushtan, A., Sprinzak, D., *et al.* (2004) Scanning electron microscopy of cells and tissues under fully hydrated conditions. *Proc. Natl. Acad. Sci. USA* **101**, 3346–3351.

Williamson, M.J., Tromp, R.M., Vereecken, P.M., Hull, R. & Ross, F.M. (2003) Dynamic microscopy of nanoscale cluster growth at the solid-liquid interface. *Nat. Mater.* **2**, 532–536.

Zheng, H.M., Claridge, S.A., Minor, A.M., Alivisatos, A.P. & Dahmen, U. (2009a) Nanocrystal diffusion in a liquid thin film observed by in situ transmission electron microscopy. *Nano Lett.* **9**, 2460–2465.

Zheng, H.M., Smith, R.K., Jun, Y.W., Kisielowski, C., Dahmen, U. & Alivisatos, A.P. (2009b) Observation of single colloidal platinum nanocrystal growth trajectories. *Science* **324**, 1309–1312.